Experimental results from a high heat flux solar furnace with a molten metal-cooled receiver SOMMER

F. Müller-Trefzer[a,*], K. Niedermeier[a], F. Fellmoser[a], J. Flesch[a], J. Pacio[b], T. Wetzel[a]

[a] *Karlsruhe Institute of Technology (KIT), Institute for Energy Technology and Safety, Hermann-von-Helmholtz-Platz 1, 76344 Eggenstein-Leopoldshafen, Germany*
[b] *Belgian Nuclear Research Centre (SCK CEN), Boeretang 200, 2400 Mol, Belgium*

Abstract

Liquid metals are promising candidates for highly efficient thermal receivers in concentrating solar power plants due to their excellent thermal conductivity. In the SOMMER (SOlar furnace with a Molten MEtal-cooled Receiver) facility at the Karlsruhe Institute of Technology (KIT), the cooling of a 10-kW thermal receiver by a lead-bismuth eutectic flow has been successfully demonstrated at high heat flux conditions in a solar furnace without any receiver damage.
The experimental results show that peak heat fluxes of up to 4 MW/m^2 can be achieved in the SOMMER facility and efficiently cooled with a liquid metal flow. In this study, the experimentally determined heat flux densities in the focal point of the solar furnace and the power input by the receiver are presented. In addition, the estimation of the thermal losses of the receiver are described and the results are discussed.

The test results from three different shutter blinds positions as well as three different inlet temperatures (200 °C, 250 °C, 300 °C) and different mass flows are presented. During the measurement campaign in the summer of 2019 the Direct Normal Irradiance (DNI) values ranged from 670 W/m^2 to 960 W/m^2. Under these conditions maximum wall temperatures of 670 °C were measured. All in all, the results prove the excellent cooling ability of liquid metals under high heat flux conditions of up to 4 MW/m^2.

Keywords: liquid metal, concentrated solar power, thermal receiver, lead-bismuth eutectic, high heat flux

1. Introduction

Previous studies have shown that further cost reductions are necessary for concentrating solar power (CSP) technology to be competetive with photovoltaics technology [1, 2]. Currently, most central receiver plants are operated with so-called 'solar salt' (60 wt% $NaNO_3$ and 40 wt% KNO_3) with operating temperatures of up to 565 °C [3]. One possible way to achieve the required cost reductions is to increase the overall efficiency of the CSP plant. This could be accomplished both by increasing the outlet temperature of the receiver and thus, the inlet temperature of the steam cycle to increase the Carnot efficiency and by increasing the receiver efficiency [4].

Using liquid metals in the thermal receiver has the potential to tackle both of these issues due to their high thermal conductivity and large operating temperature range [5, 6]. In a techno-economic analysis, Fritsch et al. [7] showed that with a single-aim point strategy, which is possible when using liquid metals in the receiver, double the heat flux density can be reached compared with molten salt resulting in up to 16% lower electricity generation costs. Additionally, liquid metals are applicable in a wide temperature range, as is shown in Table 1.

Table 1: Temperature range and physical properties averaged in the temperature range of 300–600 °C (1 bar)

	T	c_p	ρ	λ	Ref.
	°C	Jkg^{-1}K^{-1}	kg m^{-3}	Wm^{-1}K^{-1}	
Sodium	98–883	1256	798	57.5	[8]
LBE	125–1670	143	10139	13.7	[9]
Solar salt	220–600	1520	1804	0.5	[10]

Sodium-cooled receivers have already been tested in Almeria, Spain, in the 1980s in a pilot-scale power plant showing high receiver efficiencies [11] and more recently, in Jemalong, Australia [12]. However, only a limited amount of experimental data is available and as, especially in the nuclear field, the general knowledge regarding liquid metal technology has improved in the last 30 years, it is time to re-evaluate liquid metal solar technology.

Therefore, the SOMMER (SOlar furnace with a Molten MEtal-cooled Receiver) facility [13, 14] at the Karlsruhe Liquid Metal Laboratory (KALLA) of the Karlsruhe Institute of Technology (KIT), was built in order to re-examine liquid metals as heat transfer fluids for CSP in a model re-

*Corresponding author
Email address: franziska.mueller-trefzer@kit.edu (F. Müller-Trefzer)

ceiver under high heat flux conditions. In the SOMMER receiver loop, lead-bismuth eutectic (LBE) is used as the working fluid. Among the liquid metals suitable for the target operating temperature range in a concentrating solar power plant (600 °C and beyond), sodium would be the first choice due to its high thermal conductivity leading to an exceptional heat transfer (Table 1). However, sodium reacts strongly with water, therefore, extensive safety measures have to be taken. Therefore, LBE was selected as a chemically less reactive model fluid for the SOMMER loop in order to investigate the general heat transfer characteristics of liquid metals in a thermal receiver and to gain experience in the operation of a model receiver with liquid metal under highly-concentrated sunlight conditions with simple safety requirements.

In the following, the set-up of the SOMMER facility (section 2), the determination of the target values (section 3) and the operation procedure of the SOMMER facility (section 4) are presented. Finally, the experimental results of the heat flux measurement, the thermal receiver power and the thermal losses are shown and discussed (section 5).

2. The SOMMER facility

The set-up of the SOMMER facility is summarized in this section. The components (the solar furnace, the liquid metal loop and the measurement setups in the focal point) are briefly described in the following sections. A detailed description was previously given by Flesch et al. [13, 14].

2.1. The solar furnace

The solar furnace arrangement is shown in Fig. 1. The solar furnace consists of a heliostat mirror (32 m^2) and a parabolic mirror (16 m^2). Both, the heliostat mirror and the focal point are horizontally aligned on the optical axis of the parabolic mirror. This configuration is also called an on-axis arrangement [15]. The heliostat mirror tracks the sun and reflects the sunlight onto the parabolic mirror, which concentrates the sunlight. A two-axis tracking system (azimuth and elevation tracking) is used. The parabolic mirror can be moved along the optical axis, which allows a shift of the focal plane as shown in Fig. 1. Two different focal planes are required one for the heat flux measurement and the other one for the receiver measurement. The measurement methods are described in detail in section 2.3 and 2.4.

The Direct Normal Irradiance (DNI) is measured by a Hukseflux DR-02 Pyrheliometer characterised by a opening half-angle of 2.5°, as proposed by the world meteorological organization [16].

Peak DNI values of 950 W/m^2 have been measured at the location of the SOMMER facility at KIT Campus North. The solar power on the receiver can be varied by adjusting the horizontal shutter blinds, which are placed between the heliostat and the parabolic mirror in the roll-up gate of the lab. The shutter blinds were adjusted by

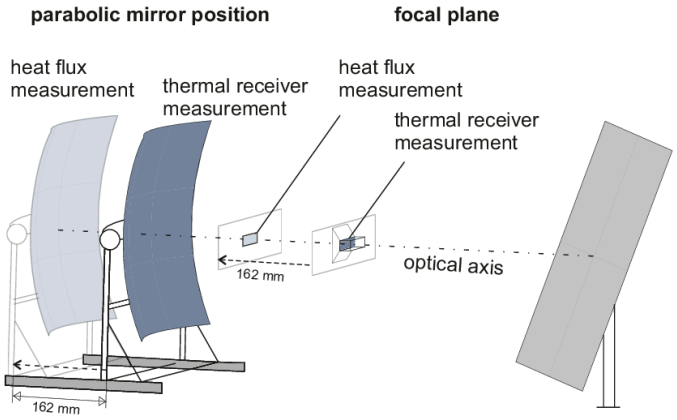

Figure 1: Solar furnace arrangement: parabolic mirror (left – adjustable along the optical axis), focal plane (center – depending on the position of the parabolic mirror) and heliostat (right) are aligned on the optical axis. Two different setups are shown, the 'thermal receiver measurement' (section 2.3) and the 'heat flux measurement' (section 2.4) setup.

moving the shaft of the shutter by 100° or 180°. Three different shutter settings were defined: 'inclined' (100°), 'horizontal' (180°) and 'without' if the shutter is fully open, as it is shown in (Fig. 2).

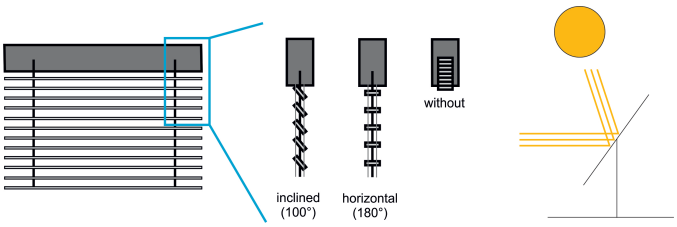

Figure 2: Different shutter settings; right: direct solar radiation deflected by the heliostat mirror, middle: different shutter positions as seen from the side, from right to left: without shutter, horizontal (180°) and inclined (100°) shutter setting, left: front view of the shutter

2.2. The liquid metal loop

Figure 3 shows a picture of the SOMMER facility. The aperture area of the thermal receiver (3), placed in the centre of a copper shield, is visible as a reflection in the parabolic mirror. On the right-hand side is the thermally insulated LBE loop (1–5).

Figure 4 presents a simplified flow diagram of the SOMMER liquid metal loop. The liquid metal is pumped by a gear pump (1) and the flow rate is measured with a Venturi nozzle. Then the LBE flow is heated up in the electric heater (2) to the favoured inlet temperature of the receiver. The pre-heated fluid enters the receiver (3), where the temperature is further increased by the power of the concentrated sunlight. In the air cooler (4) the temperature is decreased to the temperature prevailing in the buffer tank of the pump (1). During downtime or in case of a failure, all the LBE is drained into the sump tank (5) and kept above melting temperature.

Figure 3: Picture of the SOMMER facility on-axis arrangement, taken by Mueller-Trefzer/KIT; 1: pump buffer tank, 2: heater, 3: receiver and copper shield (front and back), 4: cooler, 5: sump tank

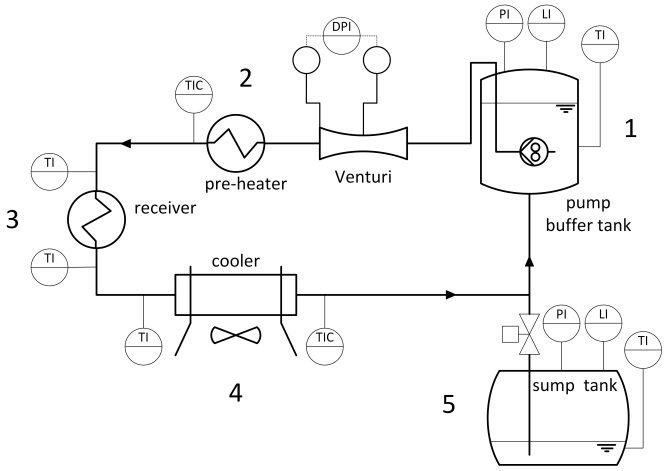

Figure 4: Flow diagram of SOMMER liquid metal loop; 1: pump buffer tank, 2: heater, 3: receiver, 4: cooler, 5: sump tank

2.3. 'Thermal receiver measurement' setup

The thermal receiver experiences a thermal power of more than 10 kW on its irradiated aperture area of 100 mm x 100 mm. It has a spiral design with 10 tubes in the focal point (Fig. 5). The receiver material is austenitic steel (1.4571) and the tubes have an outer diameter of 10 mm and a wall thickness of 0.5 mm. In the tube – with a heated tube length of approximately 1 m – the fluid was heated up by a maximum of 180 K in the experiments. The spiral design was chosen to achieve similar Nusselt and Reynolds numbers as in a reference receiver of 42 MW at full load, as described by Flesch et al. [14]. The receiver surface is coated with a 40 µm layer of Pyromark 2500. Spectral optical properties of the absorptive paint are described in the literature [17, 18]. The temperatures at the inlet and outlet of the receiver are determined with thermocouples that are placed in the flow. The thermal receiver is surrounded by a copper shield in order to avoid excessive heating of the thermal insulation around the receiver.

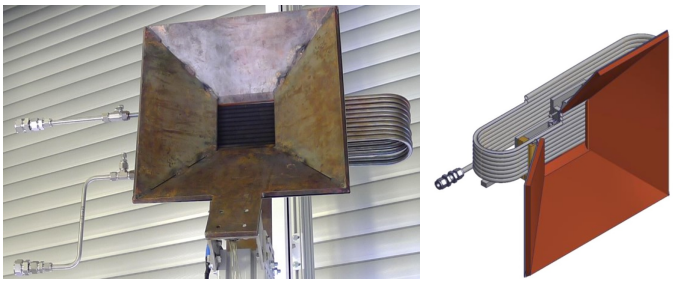

Figure 5: Left: picture of thermal receiver without insulation and copper shield, taken by Flesch/KIT; right: CAD model of the spiral receiver [14]

The heliostat mirror is continously tracking the sun during the day. During the 'thermal receiver measurement', the heliostat mirror continued to track every 10 s, whereas during the 'heat flux measurement' the heliostat mirror was stopped for the duration of the measurement (16 s). The stepwise adjustment of the heliostat by the hydraulic system would lead to larger errors due to the tracking compared with the deviation caused by stopping the heliostat for a short time (up to 16 s) during the 'heat flux measurement'.

In order to check that the deviation is small, an infrared camera monitors the receiver to make sure that the focal point is always within the aperture. The calibrated infrared camera (InfraTec VarioCam (R) HD head 800) is used both as a safety feature during operation and for the estimation of the heat losses.

The heat flux measurement cannot be conducted in the same focal area as the thermal receiver is located, therefore, the parabolic mirror is fixed on a track system and can be moved depending on the measurement. The parabolic mirror is movable along the axis of symmetry of the paraboloid, as shown in Fig. 1. For the two measurement setups the parabolic mirror is moved for 162 mm but could be moved up to 450 mm.

The mirror is positioned such that the receiver is in the focal plane of the paraboloid when measuring the absorbed thermal power in the LBE flow in the thermal receiver.

This measurement in this position is further referred to as 'thermal receiver measurement' setup.

2.4. 'Heat flux measurement' setup

In order to determine the heat flux distribution in the focal point, the mirror is moved backwards away from the receiver and thus, also the focal point is moved backwards to a position between the parabolic mirror and the receiver. This is referred to as the 'heat flux measurement' setup in the following. This focal plane is then scanned by a heat flux micro sensor (HFM) on 'spiral' paths (rotational and superimposed linear motion) to measure the heat flux distribution. During the 'heat flux measurement', a linear motor moves forwards into the focal plane and backwards out of the focal plane. Figure 6 visualizes the spiral paths during the forward measurement. The

overall measurement time for the forward movement is 8 seconds. In this time, the sensor moves with approximately 1.8 revolutions per second and a linear speed of 0.02 m/s, resulting in approximately 15 revolutions in each forward or backward measurement. The data is gathered at a sample rate of 6 kHz. The total time for both the forward and the backward measurement is 16 seconds.

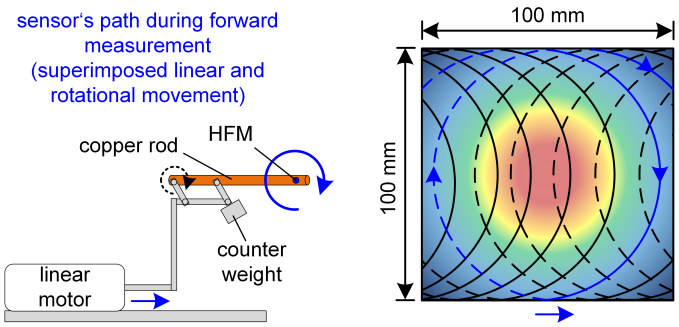

Figure 6: Schematic illustration of the spiral paths of the sensor during the forward measurement of the heat flux distribution

For both forward and backward measurement the heat flux density distribution is determined and then averaged. In Fig. 7 the setup for both the 'heat flux measurement' and the 'thermal receiver measurement' is shown.

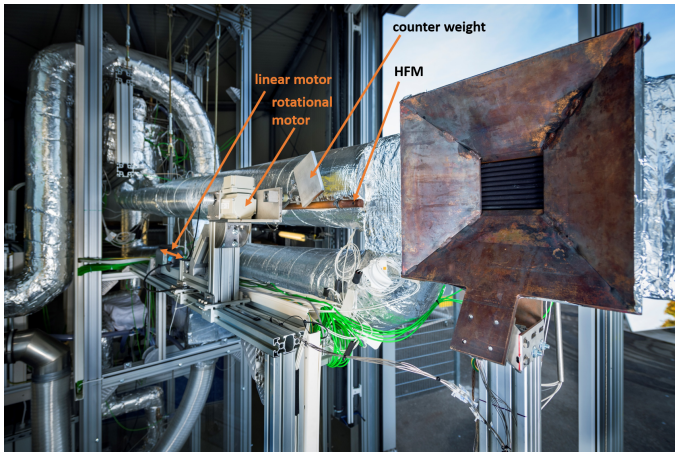

Figure 7: Picture of the SOMMER facility, taken by Bramsiepe/KIT; left: measuring device for determining the heat flux distribution with sensor at the tip of the copper rod; right: receiver

In the SOMMER facility a HFM-6D/H heat flux micro sensor by Vatell, with a short response time of 300 µs, is used. The sensor is able to operate at temperatures up to 800 °C and is coated with Pyromark 2500. The sensor was calibrated up to 2 MW/m^2 taking into account the Pyromark, 2 MW/m^2 corresponds to the expected maximum power of a two-peak heat flux distribution on the receiver. This two-peak heat flux distribution was measured and reported in 2017 [14] and was, at that time, caused by canting issues of the heliostat mirror facets. However, over time, the canting of the facets was reduced as the facets flattened, which was leading to only one peak in the heat flux distribution with a significantly higher peak heat flux.

3. Determination of target parameters

The target parameters $\dot{Q}_{\text{incident}}$, $\dot{Q}_{\text{absorbed}}$, $\dot{Q}_{\text{receiver}}$ and $\dot{Q}_{\text{losses}}$ are defined in the following.

3.1. Solar power measured by the heat flux sensor, $\dot{Q}_{incident}$

The incoming solar power $\dot{Q}_{\text{incident}}$ is determined with the heat flux measurement device developed for the SOMMER furnace, as described in 2.4. The solar power is calculated from the sum of measured heat fluxes $\ddot{q}_i$ at discrete points on the receiver surface multiplied by their covered surface area s_i of each measuring point, as represented by Eq. (1).

$$\dot{Q}_{\text{incident}} = \sum_{i=1}^{n} s_i \ddot{q}_i \tag{1}$$

For this calculation a rectangular regular grid with a horizontal resolution of 2 mm and a vertical resolution of 1 mm is used for the 100 mm x 100 mm irradiated surface of the thermal receiver. The values of the grid are obtained by interpolation from the measured values.

3.2. Absorbed thermal power of receiver, $\dot{Q}_{absorbed}$

The thermal power absorbed in the receiver $\dot{Q}_{\text{absorbed}}$ can be calculated by integrally determining the power introduced into the fluid $\dot{Q}_{\text{receiver}}$ and also taking into account heat losses $\dot{Q}_{\text{losses}}$. This results in Eq. (2).

$$\dot{Q}_{\text{absorbed}} = \dot{Q}_{\text{receiver}} + \dot{Q}_{\text{losses}} \tag{2}$$

3.3. Thermal power of receiver, $\dot{Q}_{receiver}$

The thermal power of the receiver $\dot{Q}_{\text{receiver}}$ is determined with the balance of the receiver's incoming and outgoing enthalpy fluid flows, as presented in Eq. (3).

$$\dot{Q}_{\text{receiver}} = \dot{m} c_p(T_{\text{bulk}}) \, (T_{\text{out}} - T_{\text{in}}) \tag{3}$$

The heat capacity of the mean bulk temperature is used (Eq. 4).

$$T_{\text{bulk}} = \frac{T_{\text{in}} + T_{\text{out}}}{2} \tag{4}$$

The mass flow $\dot{m}$ is measured using a venturi nozzle after the gear pump as can be seen in Fig. 4. The heat capacity of the LBE in J kg^{-1}K^{-1} is calculated using Eq. (5) [9].

$$c_{\text{p}} = 164.8 - 3.94 \cdot 10^{-2} \cdot T + 1.25 \cdot 10^{-5} \cdot T^2 - 4.56 \cdot 10^{5} \cdot T^{-2} \tag{5}$$

The inlet and outlet temperatures T_{in} and T_{out} are measured with type-K thermocouples in the LBE flow.

3.4. Thermal losses $\dot{Q}_{losses}$

The thermal losses are being quantified in this study with the aim to analyse the different loss terms that are present in the experimental setup and to validate the difference between the thermal power of the receiver $\dot{Q}_{\mathrm{receiver}}$ and the solar power measured by the heat flux sensor $\dot{Q}_{\mathrm{incident}}$.

For the evaluation of the thermal losses, a generic relation is defined. It is assumed, that both linear (conduction and convection) and non-linear (radiation) losses are present at the aperture area of the receiver A_{ap} and only linear losses (mainly conduction) at the insulated remaining parts A_{re} of the receiver's surface. The heat losses resulting from a non-ideal absorptivity of the receiver's coating are negected here, as the same coating is applied to the heat flux sensor and the receiver. Thus, it is assumed that the losses due to the non-ideal absorptivity of the coating are in the same range and can thus be neglected here. It is assumed that the temperature of receiver and sensor is comparable. The empirical correlation is presented in Eq. 6, where zero losses are assumed at 300 K.

$$\begin{aligned}\dot{Q}_{\mathrm{losses}} &= \dot{Q}_{\mathrm{losses,ap}} + \dot{Q}_{\mathrm{losses,re}} \\ &= A \cdot \left(\frac{T_{\mathrm{infra}}}{300\mathrm{K}} - 1\right) + B \cdot \left[\left(\frac{T_{\mathrm{infra}}}{300\mathrm{K}}\right)^4 - 1\right] \\ &+ C \cdot \left(\frac{T_{\mathrm{bulk}}}{300\mathrm{K}} - 1\right)\end{aligned} \tag{6}$$

For the estimation of the heat losses of the aperture, the temperature from the infrared camera (T_{infra}) and for the remaining part of the receiver, the mean of the inlet and outlet temperatures of the receiver (T_{bulk}) is taken as a reference as those are the relevant temperatures of the respective surfaces.

To represent the reference temperatures as dimensionless temperatures it is referred to a temperature of 300 K; at this temperature level the losses are expected to be very small.

The losses are weighted according to their surface area. The fraction of the aperture area (A_{ap}) and the remaining surface area (A_{re}) and the overall surface area of the receiver (A_{rec}) are determined from the dimensions of the receiver. The coefficients A, B and C are obtained with least-squares fits in two dedicated isothermal experiments without sun, they are explained and evaluated in section 5.1.

In these isothermal experiments, the thermal losses $\dot{Q}_{\mathrm{losses}}$ are determined from the temperature difference between inlet and outlet of the receiver, assuming negligible changes of the ambient temperature (Eq. (7).

$$\dot{Q}_{\mathrm{losses}} = \dot{m} \cdot c_p(T_{\mathrm{bulk}}) \cdot (T_{\mathrm{in}} - T_{\mathrm{out}}) \tag{7}$$

3.5. Measurement uncertainties

The uncertainties of measurement were determined as follows. For primary variables, such as the temperature, the random standard measurement uncertainty is related to the fluctuation of the signal caused by physical mechanisms (e.g. turbulence) or electrical interferences on the transmission cables. A large sampling time can minimize these influences. The 'thermal receiver measurement' lasted 180 s at a sampling rate of 2 Hz. This random standard measurement uncertainty is combined with the systematic standard measurement uncertainty obtaining a combined uncertainty. The temperature of the fluid entering the receiver has a mean combined uncertainty of 0.12 K. The maximum combined uncertainty is about 0.15 K. The mean combined uncertainty of the outlet temperature is slightly higher with 0.3 K. For the reference temperature determined by the IR-camera a measurement uncertainty of 20 K are assumed. The mass flow rate shows a combined uncertainty of 1% on average with a maximum of 1.1%.

Secondary variables which depend on a set of n primary variables, assuming that these contributions are independent from each other, are determined according to the equation given in Ref. [19] for the combined standard uncertainty for uncorrelated input quantities.

The heat flux sensor was calibrated in the solar simulator at DLR in Cologne. The combined uncertainty of the heat flux on the receiver $\dot{Q}_{\mathrm{incident}}$ is below 5.5% for more than 95% of the measurements. The mean combined uncertainty of all measurements is 3.2%.

4. Operation procedure of the SOMMER facility

In the following, the different measurement settings as well as the stability of the SOMMER loop during both a single measurement and the entire measurement campaign are presented.

4.1. Measuring matrix

Table 2 shows the measuring matrix of the experiments performed in the SOMMER facility from June 26th 2019 till September 19th 2019. The inlet temperature was adjusted as well as the shutter setting and the LBE mass flow. The first twelve cases are shown in detail in Table 2 exemplarily. The other measurements were performed in the same way. However, at an inlet temperature of 250°C no measurements were carried out at the lowest mass flow and without shutter. At an inlet temperature of 300°C and without shutter only measurements for the two largest mass flows were carried out.

Each measurement was repeated up to 5 times (min. 3 times) when the system reached steady-state and each measurement was executed for 180 s. The results displayed in the following are averaged results from this time period. After each measurement the heat flux density distribution was determined as explained before. When both the outward and return movement are considered, the measurement takes 16 seconds in total.

Table 2: Measuring matrix

No.	T_{in}	Shutter setting	Mass flow
	°C	–	kg/s
1-4	200	inclined (100°)	0.76/0.58/0.40/0.32
5-8	200	horizontal (180°)	0.76/0.58/0.40/0.32
9-12	200	without	0.77/0.58/0.41/0.34
13-16	250	inclined (100°)	0.74/0.55/0.39/0.31
17-20	250	horizontal(180°)	0.74/0.56/0.38/0.31
21-23	250	without	0.73/0.56/0.38
24-27	300	inclined (100°)	0.7/0.53/0.36/0.29
28-31	300	horizontal (180°)	0.72/0.55/0.38/0.29
28-29	300	without	0.71/0.54

4.2. Stability of the SOMMER loop

The mass flow is controlled via the rotation speed of the gear pump in the pump buffer tank. The temperature of LBE has a small impact on the mass flow. Furthermore, the inlet temperature of the receiver is very stable even during highly fluctuating DNI as shown in Fig. 8.

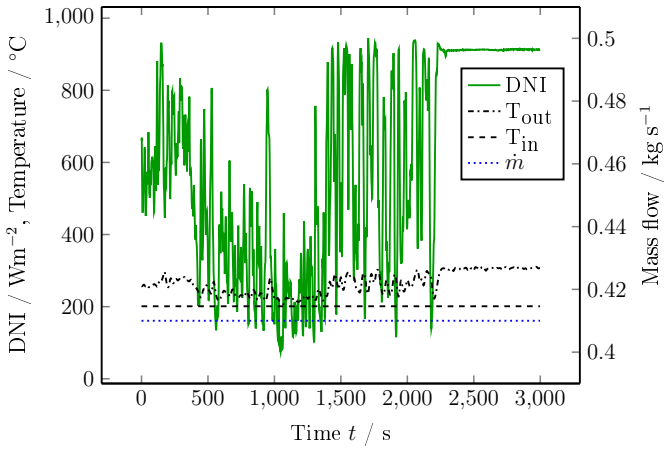

Figure 8: Stability of loop during 50 min of operation on a day with strongly varying DNI. The temperature T_{in} and T_{out} are measured in the fluid at the receiver inlet and outlet.

For these highly fluctuating DNI, the temperature fluctuations at the outlet of the receiver and thus, at the inlet of the cooler the temperature varies up to 100 K. However, the control of the cooler achieves a reduction of these temperature fluctuations to a maximum temperature difference of 20 K at the outlet of the cooler. This flow is then entering the pump buffer tank. The volume ratio of LBE in the buffer tank to the volume in the LBE loop plays an important role as well. In the SOMMER facility the volume ratio of the buffer tank to the LBE loop is about 6. Therefore, the temperature in the buffer tank changes only by +/- 0.8 K and at the entrance of the receiver by only +/- 0.1 K.

The experiments are done in clear sky conditions. Therefore, during experiments the relative standard deviation of the DNI does not change by more than 1.5% during the 'thermal receiver measurement'. The receiver inlet temperature does even not change more than 0.2% at a maximum and less than 0.1% on average. On average the relative standard deviation of the DNI changes less than 1.1%. During the 'heat flux measurement' the relative standard deviation of the DNI does not differ by more than 1.5% at a maximum and 1% on average.

Figure 9 shows the determined powers in all of the performed experiments during the measurement campaign, which are the measurements shown in Table 2 including their 3–5 repetitions. They prove the stability of the overall measurement campaign, as no systematic drift of the determined values with advancing time is noticable for the determined target parameters of the experiments.

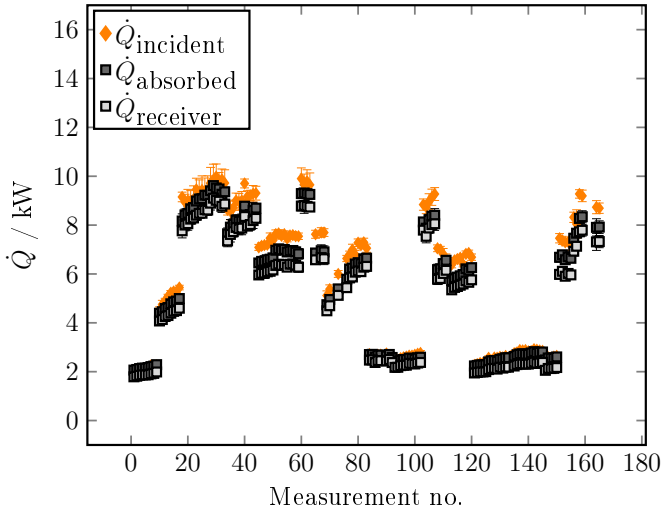

Figure 9: Stability of the evaluated parameters along the numbers of measurements of the three-month campaign (33 measuring points including their 3–5 repetitions)

5. Experimental results

The experimental results obtained from varying the shutter setting, the mass flow and the inlet temperature are presented. Firstly, the estimation of the thermal losses in isothermal no-sunlight conditions are presented. Secondly, the DNI values are compared for the two corresponding measurements ('heat flux measurement' and 'thermal receiver measurement'). Thirdly, the 'heat flux measurement' results are discussed. Finally, the comparison of the 'heat flux measurement' and 'thermal receiver measurement' results is presented.

5.1. Thermal losses estimation

In order to evaluate the thermal losses of the thermal receiver, isothermal experiments were performed between 200°C and 420°C without incident sunlight.

Two experimental settings were chosen to determine the coefficients for the empirical correlation shown in Eq. 6:

experiments with open aperture area and experiments with closed aperture area (Fig. 10).

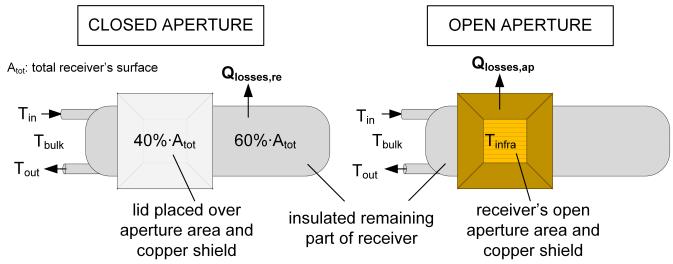

Figure 10: Scheme of heat losses experiments with closed and open aperture are showing the ratios of the receiver surface areas

The results of the heat loss measurements are shown in Fig. 11. It is noticeable that the heat losses are only 20% higher with open aperture compared with a closed aperture. Consequently, in this no-sun case most of the heat is lost through the insulated part of the receiver. This is mainly due to the fact that SOMMER is a small-scale experiment and therefore the volume to surface ratio is disadvantageous compared to a receiver in a commercial facility. It is also due to the receiver design, a spiral tube, which is flowed horizontally from top to bottom resulting in large surface area. The heat losses determined during off-sun conditions cannot be simply applied to the on-sun conditions. Therefore from these two experiments, the losses at the aperture area (including copper shield) and the losses of the rest of the receiver are derived.

Firstly, the losses of the remaining part of the receiver are assessed to determine the coefficient C in the fit function (Eq. 8).

$$\dot{Q}_{\mathrm{losses,re,fit}}(T_{\mathrm{bulk}}) = C \cdot \left(\frac{T_{\mathrm{bulk}}}{300\mathrm{K}} - 1 \right) \tag{8}$$

These losses are determined from the experiments with closed aperture area. As the aperture area takes up 40% of the overall surface, only 60% of the overall losses are taken into account for estimating the losses of the remaining insulated part of the receiver, assuming that the heat is lost uniformly at the surface. With these 60% of the heat losses, the fit factor C is determined, taking the mean bulk temperature in the receiver as a reference temperature (Eq. 9).

$$\dot{Q}_{\mathrm{losses,re}} = 0.6 \cdot \dot{Q}_{\mathrm{losses,closed}} \tag{9}$$

Secondly, the heat losses of the aperture area are derived to get coefficients A and B in the fit function (Eq. 10).

$$\dot{Q}_{\mathrm{losses,ap,fit}}(T_{\mathrm{infra}}) = A \cdot \left(\frac{T_{\mathrm{infra}}}{300\mathrm{K}} - 1 \right) + B \cdot \left[\left(\frac{T_{\mathrm{infra}}}{300\mathrm{K}} \right)^4 - 1 \right] \tag{10}$$

The losses of the aperture area are determined from the experiments with open aperture area substracting the losses of the remaining insulated part as determined before, which was calculated before (Eq. 11). It is assumed that the losses at the front, irradiated side of the aperture area (including copper shield) are dominating and the losses of the back side of the copper shield, which is insulated for the most part of its surface, are neglected.

$$\dot{Q}_{\mathrm{losses,ap}} = \dot{Q}_{\mathrm{losses,open}} - C \cdot \left(\frac{T_{\mathrm{bulk}}}{300\mathrm{K}} - 1 \right) \tag{11}$$

The results are shown in Fig. 11 and Table 3.

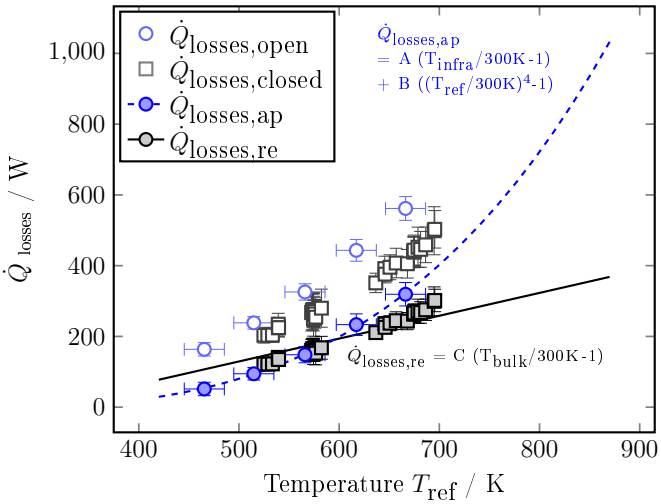

Figure 11: Thermal losses for different reference temperatures - with and without an insulating lid on the receiver aperture area; fit of experimental data according to Eq. 8 and 10 in order to determine the fitting parameters A, B and C

Table 3: Fit coefficients for thermal losses function (Eq. 6)

A / W	B / W	C / W
-40	15.9	193.8

5.2. DNI during experiments

As described in sections 2.3 and 2.4 there are two setups for the 'heat flux measurement' and the 'thermal receiver measurement', which cannot be performed at the same time. Hence, comparable conditions concerning direct normal irradiance are crucial. Figure 12 shows the DNI during the 'thermal receiver measurement' and the corresponding DNI during the 'heat flux measurement'. All corresponding measurements do not deviate more than about 5% from the bisector. 94% of all measurements are within +/- 2% of the bisector. In the following only those measurements where the DNI of the heat flux measurement and the 'thermal receiver measurement' do not differ more than 2% are considered.

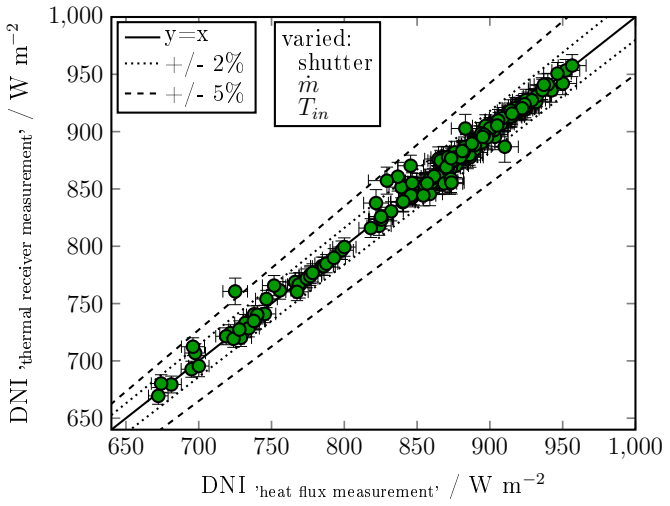

Figure 12: Comparison of DNI during 'thermal receiver measurement' and corresponding 'heat flux measurement'. The error bars refer to the combined measurement uncertainty determined from the standard deviation of the DNI measurements and the instrumentation error. Data of all measurements are shown in Table 2.

5.3. 'Heat flux measurement' results

During the experimental campaign, a maximum heat flux density of $\approx 4\,\mathrm{MW/m^2}$ was measured in the SOMMER facility. The corresponding thermal receiver measurement was carried out for an inlet temperature of 250°C, a mass flow of 0.73 kg/s and a DNI of $\approx 900\,\mathrm{W/m^2}$. So far liquid metal-cooled receivers have only been operated up to a maximum heat flux of 2.5 MW/m^2 [12]. The corresponding measured heat flux density distribution is presented in Fig. 13.

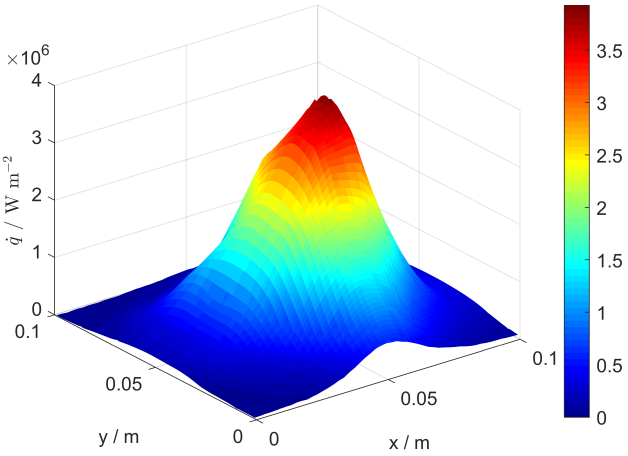

Figure 13: Maximum measured heat flux density without shutter and a DNI of $\approx 900\,\mathrm{W/m^2}$; $T_{\mathrm{in}} = 250$°C; measurement no. 21

However, it has to be noted that the calibration of the sensor has only been performed up to maximum values of 2.1 MW/m^2. At the start-up of the solar furnace, two focal points were determined due to the canted heliostat mirrors, as reported by Flesch et al. [14]. On this basis, the corresponding maximum value to be calibrated was then determined. However, in the measurement campaign presented in this study, both focal points superimposed into one due to aging and thus reducing the canting effects of the heliostat mirrors. Therefore, the values determined by the heat flux sensor are outside the calibrated range.

At a maximum heat flux of 4 MW/m^2 the peak wall temperature of the front, irradiated surface of the receiver was 580°C, determined by an infrared camera as described in section 2.4. The maximum measured wall temperature during the campaign was about 660°C for an inlet temperature of 250°C and a mass flow of 0.38 kg/s without the shutter.

Heat transfer coefficients were not estimated in the SOMMER facility. Previous numerical work [20] showed that the integral Nusselt number of a non-uniformly heated flow is quite similar to the one on a uniformly heated flow, however, the local Nusselt number resulting from a non-uniform heat flux leads to comparably higher wall temperatures. Thus, at the Karlsruhe Liquid Metal Laboratory, a dedicated setup is currently put into operation to investigate the heat transfer coefficients in a liquid metal flow under non-uniform heat flux conditions [21].

Figure 14 represents the power measured by the sensor $\dot{Q}_{\mathrm{incident}}$ as a function of the DNI for different shutter settings. Highest powers are obtained if the shutter is completely open. The less light that passes through the shutter, the lower the power measured by the sensor, with the shutter setting 100° corresponding to the least amount of light passes through.

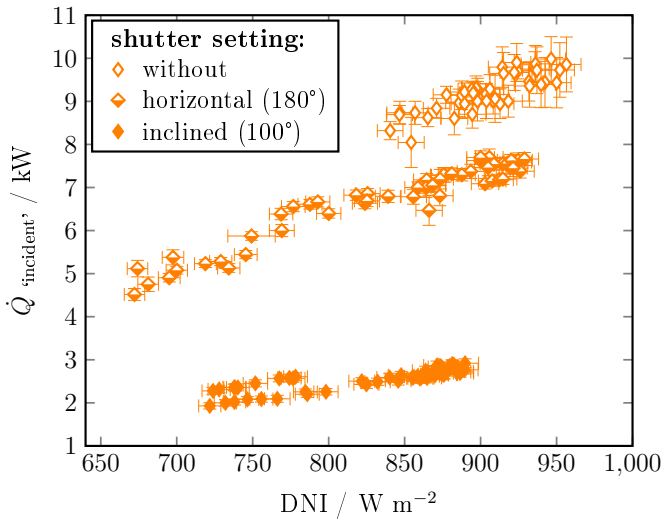

Figure 14: Dependence of the thermal power, measured by the HFM sensor, on the DNI for different shutter settings

With a shutter setting of 180° or 100° the power measured at the sensor is only about 80% or 30%, respectively, compared to measurements without the shutter. It can be seen that the power of the 'heat flux measurement' ($\dot{Q}_{\mathrm{incident}}$) for all shutter settings correlates with the DNI in a way that the measured power increases with increasing DNI.

For the shutter setting of 100° and a DNI between 720 W/m^2 and 820 W/m^2, there are two sets of experimental data which deviate up to 15%. The lower values were obtained on the 26th of June, 2019, and the higher four weeks later, on the 26th of July. Since similar DNI were measured at similar points in time, the time of day can be excluded as the cause for the sensor power difference. We identified potential reasons for this deviation. Firstly, it it possible that the shutter adjustment was not done correctly on one of those two days. However, we can not see any deviations for this shutter adjustment of 100° for the other five measuring days (DNI values from 820 W/m^2 to 900 W/m^2). Also, it cannot be excluded that dust on the heliostat has an effect on the receiver performance, even though the heliostat was cleaned regularly. However, no such deviations were found in the other measurements. Furthermore, on the 26th of June a major Sahara dust event with an otherwise clear atmosphere took place. According to Blanc et al. [22], this can lead to higher circumsolar contributions. These higher circumsolar contributions do not significantly influence the measurement of the pyrheliometer due to its opening half-angle of 2.5°, however, it can influence the measurement in the focal point of the solar furnace. As the SOMMER solar furnace can be considered a dish system, its half-angle is expected to be lower than 1.6° [22] and thus, a significantly higher sensitivity to the cicumsolar distribution is expected.

5.4. Comparison of heat flux measurement and thermal receiver results

In Fig. 15 the correlation between DNI and the power measured in the solar furnace is presented. The following experimental results (Table 2) are selected from the measuring matrix: constant shutter setting at 100°, varied inlet temperature into the receiver, varied mass flow (measurement No. 1-4, 13-16 and 24-27). The lightgrey filled squares show the measured power in the liquid metal flowing through the receiver $\dot{Q}_{\text{receiver}}$, which is determined by the inlet and outlet temperature according to Eq. 3. In order to compare the power measured by the sensor ($\dot{Q}_{\text{incident}}$, filled diamond) with the receiver power $\dot{Q}_{\text{receiver}}$, the heat losses $\dot{Q}_{\text{losses}}$ must be taken into account. This is represented by $\dot{Q}_{\text{absorbed}}$ (Eq. 2) as the darkgrey filled squares. Figure 15 shows that the power measured with the sensor matches well with the absorbed thermal power $\dot{Q}_{\text{absorbed}}$ in the receiver.

Here again, as already shown in Fig. 14, at low DNI values (700 to 800 W m^{-2}) the measured thermal power $\dot{Q}_{\text{incident}}$ differs about 12% to 15%. This phenomena can be observed not only for the sensor measurements but also for the receiver measurements $\dot{Q}_{\text{receiver}}$. Thus, at the same day, the measured sensor power is in very good agreement with the corresponding absorbed thermal power in the receiver $\dot{Q}_{\text{absorbed}}$. It follows that the cause of the difference in the measured power in the solar furnace at comparable DNI values for different days is probably not a measurement-related problem.

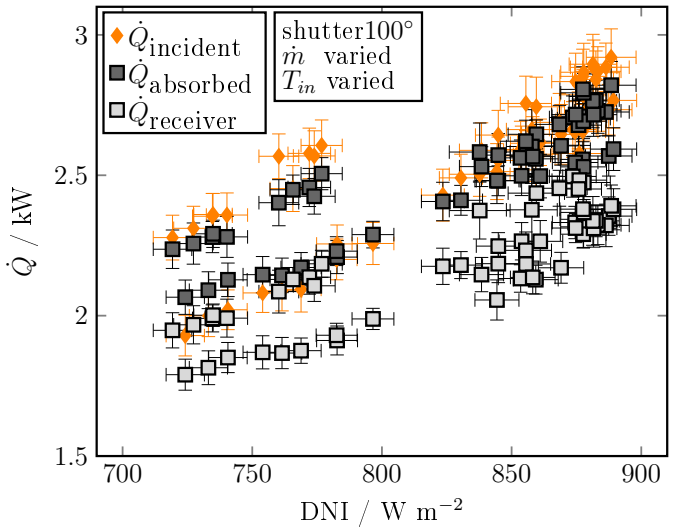

Figure 15: Measured thermal power by the heat flux sensor and in the thermal receiver, with and without including losses for varying mass flow and inlet temperature settings for the shutter setting 'inclined' (100°)

In Fig. 16 the measurements of the heat flux ($\dot{Q}_{\text{incident}}$, incoming solar power) and the corresponding thermal receiver ($\dot{Q}_{\text{absorbed}}$, absorbed thermal power) are compared. The thermal power in the focal point determined with the heat flux sensor device is slightly overestimated compared to the absorbed thermal power. However, the two measurements never differ by more than 15%.

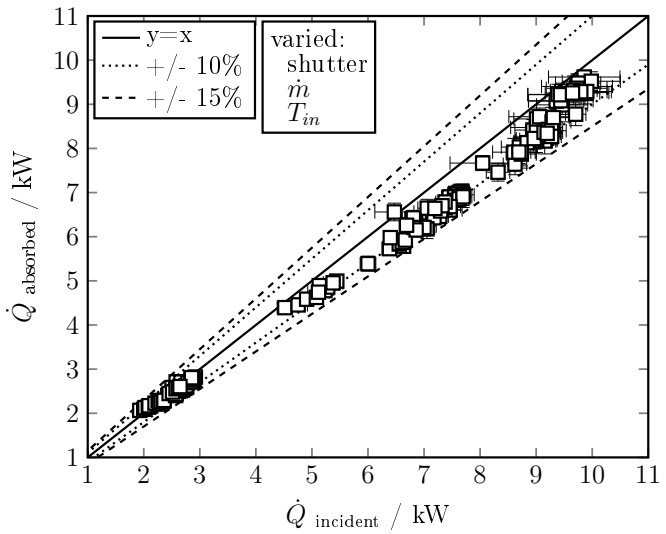

Figure 16: Comparison of the heat flux measurements ($\dot{Q}_{\text{incident}}$) and the thermal receiver results ($\dot{Q}_{\text{absorbed}}$). Data of all measurements are shown in Table 2.

As both the sensor and the receiver are coated with Pyromark 2500, the influence of different absorption behavior of sunlight is assumed to be negligible. Also the DNI never deviates more than 2% at the time of the two measurements. However, in the following other possibilities are

being considered which could be responsible for this difference. Since the sensor was used outside the previously calibrated range, its measurement could cause greater inaccuracy than expected. To rule out this influence, the sensor would have to be re-calibrated for higher maximum flux densities. Nevertheless, since all the measured sensor and receiver data show very good agreement, the sensor power is plausible in general. It is also possible that the heat losses of the receiver were not estimated sufficiently. In order to obtain a higher measurement reliability for the heat losses, additional measurements would have to be carried out at isothermal conditions for temperatures higher than 400°C.

6. Conclusions

The SOMMER setup consists of a solar furnace and a liquid metal loop, which is operated with lead-bismuth eutectic (LBE). In the focal point of the solar furnace a spiral receiver is cooled with LBE. Thanks to the movable parabolic mirror of the solar furnace, for each receiver test the heat flux density can be determined by a heat flux microsensor in the focal point as well. The SOMMER facility was successfully put into operation and the results are presented in this paper. In the following the main conclusions are summarized.

- A solar furnace with a liquid metal-cooled receiver has been successfully operated under varying sunlight conditions and extremely high heat flux densities up to 4 MW/m^2. With this heat flux density on the receiver, the receiver wall, which was irradiated by the sun, did heat up to 580°C for a mass flow of 0.73 kg/s and an inlet temperature of 250°C.
- Heat transfer coefficients were not determined in this work. A previous numerical study [20] indicates differences in the local Nusselt number obtained with a non-uniform heat flux boundary condition compared with a uniform one. Therefore, a dedicated setup is currently put into operation [21].
- During the measurement campaign a maximum wall temperature of about 660°C was obtained for an inlet temperature of 250°C and a mass flow of 0.38 kg/s without the shutter.
- The LBE flow has successfully cooled the model receiver under these demanding heat flux conditions without any failure. Up until now, liquid metal receivers have been operated with heat fluxes up to a maximum of 2.5 MW/m^2 [12].
- The SOMMER facility has been steadily operated under varying sunlight conditions.
- The heat flux density and the absorbed power in the receiver cannot be measured simultaneously. The approach to perform the two measurements consecutively has proven to be successful, as in 94% of all experiments the DNI did not deviate more than +/- 2%.
- The losses in the receiver were estimated by performing isothermal tests without sun. The losses combined with the absorbed power of the receiver are in good accordance with the power measured at the sensor in the solar furnace. The deviation is less than 15% for all measurements.
- The determined thermal losses ($\dot{Q}_{\mathrm{losses}}$) vary between 0.21 kW and 0.70 kW for thermal powers from 1.8 kW to 9.1 kW measured integrally in the receiver ($\dot{Q}_{\mathrm{receiver}}$).

Acknowledgement

The authors wish to acknowledge the support and funding of the Helmholtz Association in the framework of the Helmholtz-Alliance LIMTECH (Liquid Metal Technology). We would like to thank M. Daubner, A. Jekel, K. Wittemann and all the students that contributed to this work. Furthermore, we would like to acknowledge the helpful discussions regarding the influence of Sahara dust with Gholamali Hoshyaripour, Bernhard Vogel and Frank Wagner of the Institute of Meteorology and Climate Research.

Nomenclature

Latin letters

c_p	Heat capacity /J kg $^{-1}$ K^{-1}
$\dot{m}$	Mass flow / kg s^{-1}
$\ddot{q}_i$	Heat flux at one measuring point / W m^{-2}
$\dot{Q}_{\mathrm{absorbed}}$	Thermal power absorbed by the receiver / W
$\dot{Q}_{\mathrm{incident}}$	Incident thermal power obtained with the HFM / W
$\dot{Q}_{\mathrm{losses}}$	Thermal losses of the receiver / W
$\dot{Q}_{\mathrm{losses,ap}}$	Thermal losses of the aperture area of the receiver / W
$\dot{Q}_{\mathrm{losses,closed}}$	Thermal losses of the experiments with closed aperture / W
$\dot{Q}_{\mathrm{losses,open}}$	Thermal losses of the experiments with open aperture / W
$\dot{Q}_{\mathrm{losses,re}}$	Thermal losses of the remaining receiver's surface / W
$\dot{Q}_{\mathrm{receiver}}$	Thermal power absorbed by the receiver including thermal losses / W
s_i	Area of one measuring point / m^2
t	Time / s
T	Temperature / K
T_{bulk}	Mean bulk temperature in the receiver / K
T_{in}	Inlet temperature at the receiver / K
T_{infra}	Mean temperature determined with the infrared camera/ K
T_{ref}	Reference temperature for determining the heat losses at the receiver/ K
T_{out}	Outlet temperature at the receiver / K
x	Coordinate along receiver width / m
y	Coordinate along receiver height / m

Greek letters

λ	Thermal conductivity / W m^{-1} K^{-1}
ρ	Density / kg m^{-3}

Acronyms

CAD	Computer-aided design
CSP	Concentrating solar power
DNI	Direct normal irradiance
HFM	Heat flux microsensor
IR	Infrared
LBE	lead-bismuth eutectic
SOMMER	Solar furnace with a molten metal-cooled receiver

References

[1] DoE, Concentrated solar power, in: SunShot Vision Study, Department of Energy, 2012, pp. 97–123.

[2] International Energy Agency, Technology Roadmap Solar Thermal Electricity, Technical Report, OECD/IEA, 2014.

[3] C. K. Ho, Advances in central receivers for concentrating solar applications, Solar Energy 152 (2017) 38–56.

[4] M. Mehos, C. Turchi, J. Vidal, M. Wagner, Z. Ma, C. Ho, W. Kolb, C. Andraka, A. Kruizenga, Concentrating Solar Power Gen3 Demonstration Roadmap, Technical Report NREL/TP-5500-67464, National Renewable Energy Laboratory (NREL), 2017.

[5] J. Pacio, C. Singer, T. Wetzel, R. Uhlig, Thermodynamic evaluation of liquid metals as heat transfer fluids in concentrated solar power plants, Applied Thermal Engineering 60 (2013) 295 – 302.

[6] N. Boerema, G. Morrison, R. Taylor, G. Rosengarten, Liquid sodium versus Hitec as a heat transfer fluid in solar thermal central receiver systems, Solar Energy 86 (2012) 2293 – 2305.

[7] A. Fritsch, C. Frantz, R. Uhlig, Techno-economic analysis of solar thermal power plants using liquid sodium as heat transfer fluid, Solar Energy 177 (2019) 155–162.

[8] H. Bomelburg, C. Smith, Sodium-NaK engineering handbook, Chapter 1 Physical Properties, Gordon & Breach, New York, 1976.

[9] OECD-NEA, Handbook on Lead-bismuth Eutectic Alloy and Lead Properties, Materials Compatibility, Thermal-hydraulics and Technologies, OECD/NEA Nuclear Science Committee Working Party on Scientific Issues of the Fuel Cycle Working Group on Lead-bismuth Eutectic, 2015.

[10] A. B. Zavoico, Solar Power Tower Design Basis Document, Technical Report SAND2001-2100, Sandia National Laboratories, 2001.

[11] D. Stahl, F. Boese, S. Kostrzewa, System and components design of a sodium heat transfer circuit for solar power plants, Electric Power Systems Research 3 (1980) 151 – 161.

[12] J. Coventry, C. Andraka, J. Pye, M. Blanco, J. Fisher, A review of sodium receiver technologies for central receiver solar power plants, Solar Energy 122 (2015) 749–762.

[13] J. Flesch, A. Fritsch, G. Cammi, L. Marocco, F. Fellmoser, J. Pacio, T. Wetzel, Construction of a test facility for demonstration of a liquid lead-bismuth-cooled 10 kW thermal receiver in a solar furnace arrangement - SOMMER, Energy Procedia 69 (2015) 1259 – 1268. International Conference on Concentrating Solar Power and Chemical Energy Systems, SolarPACES 2014.

[14] J. Flesch, K. Niedermeier, A. Fritsch, D. Musaeva, L. Marocco, R. Uhlig, E. Baake, R. Buck, T. Wetzel, Liquid metals for solar power systems, IOP Conference Series: Materials Science and Engineering 228 (2017) 012012.

[15] J. B. Gálvez, S. M. Rodríguez, E. Delyannis, V. G. Belessiotis, S. C. Bhattacharya, S. Kumar, SOLAR ENERGY CONVERSION AND PHOTOENERGY SYSTEMS Thermal Systems and Desalination Plants, Volume I, Eolss Publishers Co. Ltd., United Kingdom, 2010.

[16] Guide to Instruments and Methods of Observation, volume I Measurement of Meteorological Variables, 2018 ed., World Meteorological Organization (WMO), Geneva 2, Switzerland, 2018.

[17] A. Ambrosini, A. Boubault, C. K. Ho, L. Banh, J. R. Lewis, Influence of application parameters on stability of pyromark® 2500 receiver coatings, AIP Conference Proceedings 2126 (2019) 030002.

[18] J. Coventry, P. Burge, Optical properties of pyromark 2500 coatings of variable thicknesses on a range of materials for concentrating solar thermal applications, AIP Conference Proceedings 1850 (2017) 030012.

[19] Joint Committee for Guides in Metrology/WG 1, Evaluation of measurement data: Guide to the expression of uncertainty in measurement, 2008.

[20] L. Marocco, G. Cammi, J. Flesch, T. Wetzel, Numerical analysis of a solar tower receiver tube operated with liquid metals, International Journal of Thermal Sciences 105 (2016) 22–35.

[21] B. Dietrich, T. Laube, L. Marocco, T. Wetzel, Heat transfer of liquid metal flow in a tube heated on the half of the circumference - concept of a test loop, in: 16th International Heat Transfer Conference (IHTC 2018), Beijing, CHN, August 10-15, 2018, volume 2018-August of *International Heat Transfer Conference*, Begell House Inc., 2018, pp. 3191–3198. 35.12.01; LK 01.

[22] P. Blanc, B. Espinar, N. Geuder, C. Gueymard, R. Meyer, R. Pitz-Paal, B. Reinhardt, D. Renné, M. Sengupta, L. Wald, S. Wilbert, Direct normal irradiance related definitions and applications: The circumsolar issue, Solar Energy 110 (2014) 561–577.